ACS APPLIED MATERIALS & INTERFACES

Research Article

www.acsami.org

Nanosize and Surface Charge Effects of Hydroxyapatite Nanoparticles on Red Blood Cell Suspensions

Yingchao Han,*[,†] Xinyu Wang,[†] Honglian Dai,[†] and Shipu Li[†,‡]

[†]Biomedical Materials and Engineering Center, Wuhan University of Technology, Wuhan 430070, P. R. China

[‡]State Key Laboratory of Advanced Technology for Materials Synthesis and Processing, Wuhan University of Technology, Wuhan 430070, P. R. China

Supporting Information

ABSTRACT: In this paper, the effects of size and surface charge of hydroxyapatite (HAP) particles on a red blood cell (RBC) suspension were studied. Results showed that the HAP particles exhibited nanosize and surface charge effects on the RBC suspension. Differing from HAP microparticles, HAP nanoparticles induced some aggregation of the RBCs in the unstructured agglutinates. HAP nanoparticles were adhered to the surface membrane of the RBCs due to their remarkably higher adsorption capacity than the HAP microparticles, resulting in the formation of a sunken appearance ("caves") on the surface membrane of the RBCs without rupturing the lipid bilayer. In the case of high negatively charged HAP nanoparticles after heparin modification, the aggregation of the RBCs induced by the HAP nanoparticles was inhibited. Such HAP nanoparticle-induced aggregation of the RBCs could be attributed to the bridging force via the electrostatic interaction between the positively charged binding sites on the HAP surface and the negatively charged groups on the surface of the RBCs. The surface charge of the HAP nanoparticles is thus a crucial factor influencing the interaction between the HAP nanoparticles and the RBCs.

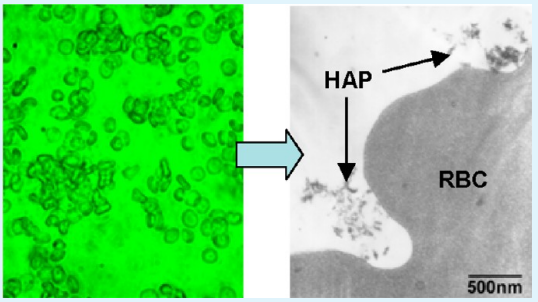

KEYWORDS: *hydroxyapatite, nanoparticle, surface charge, red blood cells, aggregation, electrostatic interaction*

1. INTRODUCTION

Nanomaterials exhibit unique physical and/or chemical properties differing substantially from those of the same material when existing in the bulk or microscale form. Many new research areas involving nanoparticles have developed in recent times for biologists to target, diagnose, and treat diseases due to the unique properties of the nanoparticles, including their small size, surface tailorability, improved solubility, and multifunctionality.[1,2] Hydroxyapatite ($Ca_{10}(PO_4)_6(OH)_2$, HAP) possesses good biocompatibility, bioactivity, osteoconductivity, nontoxicity, noninflammatory behavior, and nonimmunogenicity. To date, HAP has extensively been used as an artificial bone substitute in different medical applications.[3] Recently, HAP nanoparticles have been paid more attention due to their specific properties differing from those of HAP in the bulk form. For example, HAP nanoparticles could enhance the densification of bulk HAP and improve the fracture toughness of HAP in its ceramic form;[4−7] nanostructured HAP ceramic exhibited improved osseointegrative properties;[8,9] nanosized HAP as a supporter could increase the efficiency of catalysts.[10]

In addition, HAP nanoparticles showed promise in such applications as carriers for delivering genes, drugs and/or proteins.[11−14] Based on the high solubility in acidic pH environment of cellular endolysosomes, the molecules adsorbed onto HAP nanoparticles could be released from the pH-sensitive HAP nanoparticles. Also, rare earth ions doped HAP nanoparticles could be utilized as fluorescent labels of cells due to their good biocompatibility and biodegradability.[15−17] For the application of HAP nanoparticles in biological systems as carriers or fluorescent labels, there is a significant chance that the nanoparticles will interact with the complicated components of blood such as blood cells on account of their size. Therefore, a study of the HAP nanoparticles to determine whether they will exhibit specific properties toward such blood components is of major importance.

Herein, due to their dominant presence in the circulatory system, red blood cell (RBC) was utilized as the target for the study of the specific properties of the HAP nanoparticles. The effects of size and surface charge of the HAP particles on the aggregation and morphology of the RBCs were investigated by optical microscopy and transmission electron microscopy (TEM). The hemocompatibility of the HAP nanoparticles was also evaluated by a hemolysis assay. Moreover, the specific adsorption capacity of the HAP nanoparticles for sialic acid (SA, a membrane component of the RBCs) was studied by an adsorption experiment. For discussing the interaction mechanism between the RBCs and the HAP nanoparticles, the adsorption of SA on the HAP nanoparticles was further analyzed by Fourier transform infrared (FT-IR) spectroscopy.

Received: June 2, 2012
Accepted: August 3, 2012
Published: August 3, 2012

2. EXPERIMENTAL SECTION

2.1. Blood Collection and Handling. Whole blood (5 mL) was withdrawn from the jugular vein of a male rabbit and put into heparinized containers. Then, the whole blood was diluted using 50 mL 0.9% NaCl solution and centrifuged for 5 min at 2500 rpm. After washing four times, 0.9% NaCl solution was added to obtain a 5% RBC suspension.

2.2. Preparation and Characterization of HAP Particles. HAP nanoparticles were prepared using a precipitation method. According to the Ca/P molar ratio of about 1.67, 120 mL of $Ca(H_2PO_4)_2$ aqueous solution of 0.9658 mmol was rapidly mixed with 100 mL of saturated $Ca(OH)_2$ aqueous solution with vigorous stirring. The precipitation was kept for 24 h and then dried by a freeze-drying method.

For the preparation of surface-modified HAP nanoparticles, the above precipitation method was also utilized. After precipitation, the sodium heparin powder was added with a resulting concentration of 0.4 mg/mL. Then, the turbid dispersion was irradiated for 6 min using a high-intensity ultrasonic probe (Institute of Acoustics, China) to obtain a transparent suspension of surface-modified HAP nanoparticles. The sample was dried by a freeze-drying method.

HAP microparticles were prepared by the citric acid sol−gel combustion method.[18]

The following techniques, TEM (H-600, HITACHI, Japan), a surface area analyzer (Gemini, MICRMERITICS, USA), FT-IR, X-ray Diffraction (XRD, D/Max-IIIA, RIGAKU, Japan), size and zeta potential analyzer (Malvern Zetasizer 3000HS, UK), were utilized for the characterization of the HAP nano- and microparticles, respectively.

The HAP particles were ultrasonically dispersed in 0.9% NaCl solution to obtain a HAP particle suspension for the following experiment.

2.3. Hemolysis Assay. 2.5 mL of a 5% RBC suspension was loaded into tube and incubated at 37 °C for 30 min. Prewarming deionized water (2.5 mL) and 0.9% NaCl solution (2.5 mL) were added to RBC suspensions as the positive and negative controls, respectively. For the experimental groups, 2.5 mL of the prewarming HAP suspensions at different concentrations (0.28 mg/mL, 0.224 mg/mL, 0.168 mg/mL, 0.112 mg/mL, 0.056 mg/mL) were mixed with RBC suspensions, respectively. All groups were incubated at 37 °C and continuously observed for 4 h.

The hemolysis% of HAP particle suspension was calculated according to the equation:

$$\text{hemolysis\%} = (OD_{sample} - OD_{negative})/(OD_{positive} - OD_{negative}) \times 100\%$$

where OD_{sample}, $OD_{negative}$, and $OD_{positive}$ correspond to the absorbance values of the experimental, negative and positive groups at 545 nm respectively.[19] The hemolysis% was tested for three independent experiments and presented in mean ± SEM.

2.4. Optical Microscopy and TEM Observations. The 5% RBC suspension was placed in a tissue culture dish and incubated at 37 °C for 1 h before adding the HAP particle suspension. After 1 h of incubation with HAP particles, the RBCs were observed using an inverted microscope (CK40, Olympus, Japan). In addition, the RBCs incubated with HAP particles for 15 min and 1 h were observed using TEM.

2.5. Adsorption of SA on HAP Nano- and Microparticles. The adsorption of SA on the HAP particles was studied using the Bialsche reagent (a mixture of 0.1 g of orcinol, 47.5 mL of 38% HCl and 1 mL of 1% $FeCl_3$, and then made up to 50 mL using distilled water) test.[20] 0.02 g of HAP particles were added to 0.9 mL acetic acid-sodium acetate buffer (0.02 M, pH 6.8) and incubated at 37 °C for 1 h. Then, 0.1 mL of SA solution was added and the mixture was sequentially incubated at 37 °C for 4 h. After centrifugation at 3000 rpm for 15 min, the supernatant of 0.5 mL was moved to another centrifuge tube and 0.5 mL of acetic acid-sodium acetate buffer and 1 mL of the Bialsche reagent were added to the supernatant. Next the mixture was heated for 12 min in boiling water and immediately cooled for 3 min in ice water. After mixing with 5 mL of 1-pentanol, the mixture was centrifuged at 1000 rpm for 10 min and the supernatant was measured at 569 nm using a microplate spectrophotometer (Thermo Labsystems, Finland). The concentration of SA in the supernatant was calculated according to the standard curve (Y = 0.007 + 0.001X, r =0.999).

2.6. FT-IR Analysis. In the Bialsche reagent test, after centrifugation at 3000 rpm for 15 min, the supernatant was removed and the sediment at the bottom of the tube was washed thrice with acetic acid-sodium acetate buffer. Then, the sediment was dried by the freeze-drying method for FT-IR analysis (Nexus, Thermo Nicolet, USA) between 400 cm^{-1} and 4000 cm^{-1}.

3. RESULTS

3.1. Characterization of HAP Particles. HAP nanoparticles (Figure S1a) consisted of 18−30 nm ×45−120 nm needle-shape particles. The heparin-modified HAP nanoparticles (Figure S1b) consisted of 10−20 nm ×40−100 nm needle-shape particles. The HAP microparticles (Figure S1c) had a similar spherical shape with a diameter of 0.15−0.3 μm. The specific surface areas of the HAP nanoparticles, heparin-modified HAP nanoparticles and HAP microparticles, were determined by the BET-N_2 adsorption method to be 139.7 m^2/g, 30.0 m^2/g and 10.9 m^2/g, respectively. According to the formula, $d = 6/\rho \bullet s$, the diameters of the HAP nanoparticles, heparin-modified HAP nanoparticles and HAP microparticles were calculated to be 13.6 nm, 63.3 and 174.5 nm, respectively. The diameters of the HAP nanoparticles and microparticles were well consistent with the TEM results. Due to the adsorption of heparin, the calculated diameter of the heparin-modified HAP nanoparticles was larger than the same diameter observed by TEM.

The XRD patterns (Figure S2) demonstrated that the polycrystalline structures of the HAP nanoparticles, heparin-modified HAP nanoparticles and HAP microparticles revealed characteristics of HAP. However, the diffraction peaks were broadened and the three major diffraction peaks of (211), (112) and (300) were observed to merge into one broad peak for HAP nanoparticles and heparin-modified HAP nanoparticles, indicating the nanocrystalline nature and the lower degree of crystallinity. The sharp and distinct diffraction peaks of the HAP microparticles verified the well-crystallization and large crystalline size.

The FT-IR spectra (Figure S3) of the HAP nanoparticles, heparin-modified HAP nanoparticles and HAP microparticles also showed the characteristics of HAP. For the pure HAP nanoparticles (Figure S3a), the vibrational bands at 962 cm^{-1}, 474 cm^{-1}, 1091 and 1049 cm^{-1}, 602 and 571 cm^{-1} were attributed to the ν_1, ν_2, ν_3, ν_4 vibrational bands of phosphate group, respectively.[21] The small sharp peaks at 3571 cm^{-1} and 631 cm^{-1} were assigned to the O−H stretching and bending vibrations, respectively, in the crystal structure of HAP. The broad peak centered at 3444 cm^{-1} was due to the O−H vibration of adsorbed water. In the case of the heparin-modified HAP nanoparticles (Figure S3b), in addition to the vibrational bands of the phosphate group and the crystal structured OH of HAP, some characteristic vibrational bands of heparin (Figure S4) were observed, such as at 3442 cm^{-1}, 1,629 cm^{-1}, 1422 cm^{-1}, 1234 cm^{-1}, 894 cm^{-1} and 818 cm^{-1}. Especially, the vibrational moving of the special $-O-SO_3^-$ group of heparin (S═O and C−O−S stretching vibrations at 1239 cm^{-1} and 900−796 cm^{-1}) provided evidence that the heparin molecules were adsorbed on the HAP nanoparticles via electrostatic interaction between the positively charged sites of HAP and the

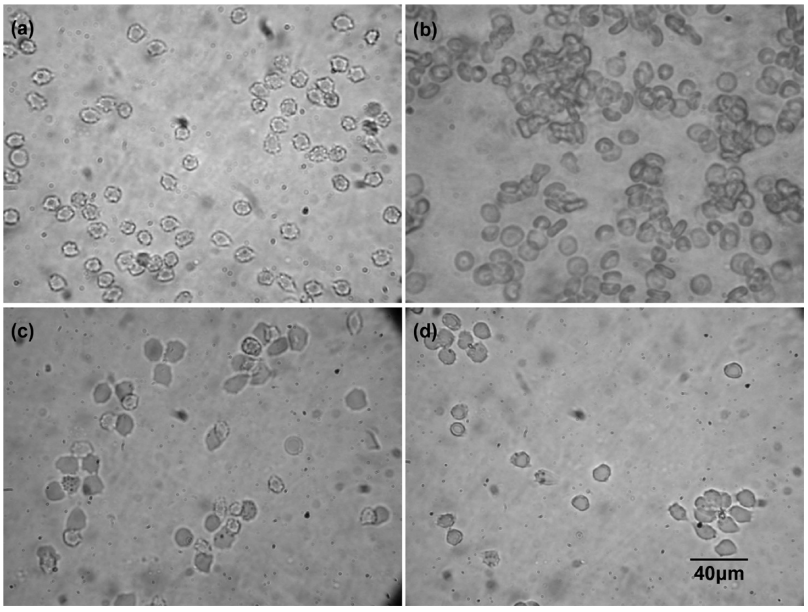

Figure 1. Light microscopy images of RBCs after 1 h incubation (a) without HAP particles and with (b) HAP nanoparticles, (c) HAP microparticles, and (d) heparin-modified HAP nanoparticles. The concentration was 140 μg/mL for each of the HAP particle groups.

negatively charged groups of heparin such as Ca^{2+} ions and $-SO_3^-$ groups. The FT-IR spectrum of the HAP microparticles (Figure S3c) exhibited much sharper peaks at 3571 cm^{-1} and 631 cm^{-1} than those of the HAP nanoparticles and heparin-modified HAP nanoparticles, indicating the higher degree of crystallinity of the HAP microparticles.

Additionally, the heparin-modified HAP nanoparticles could be well dispersed in aqueous solution and the stability of the suspension was much enhanced with the aid of heparin. The intensity-averaged particle size of the heparin-modified HAP nanoparticles was about 80 nm and the corresponding zeta potential was about −50.0 mV (Figure S5). However, the pure HAP nanoparticles and HAP microparticles were easily aggregated in aqueous solution and exhibited large sizes in aggregations (about 1 and 0.6 μm, respectively). The zeta potentials were about −7.3 mV and −17.7 mV for the pure HAP nanoparticles and HAP microparticles, respectively.

3.2. Hemolysis Assay and Optical Microscopy Observations. During the incubation experiments of the RBCs with HAP particles, hemolysis was not observed for all three kinds of HAP particles, indicating that the nanosize and high negative surface charge of the HAP particles did not influence their hemocompatibility. However, the erythrocyte sedimentation was accelerated because of the HAP nanoparticles, showing a dependence on the amount of the HAP nanoparticles. Taking high negatively charged HAP nanoparticles as an example (Figure S6), the erythrocyte sedimentation rate was increased along with the rising concentration of the HAP nanoparticles. At low concentrations of 28−56 μg/mL, the erythrocyte sedimentation rate was similar to that of the negative control group over a period of 240 min. However, a significant difference in erythrocyte sedimentation rate appeared after 60 min of incubation time with 112−140 μg/mL of HAP nanoparticles. The calculated hemolysis% of the 140 μg/mL HAP nanoparticles after 60 min was 0.09 ± 0.06, indicating the excellent hemocompatibility of these particles.

Figure 1 shows the light microscopy images of RBCs incubated with HAP particles for 1 h. After 1 h of incubation with the HAP nanoparticles, obvious RBC aggregations were observed as rounded and compressed clumps (Figure 1b). On the contrary, the HAP microparticles were not found to have evident effect on the RBCs after 1 h of incubation (Figure 1c). Moreover, in the case of the highly negatively charged HAP nanoparticles (Figure 1d), the RBC aggregations were significantly lower compared to that of the HAP nanoparticles.

3.3. TEM observations. TEM observations further revealed the interaction between the RBCs and the HAP particles. After 1 h of incubation with the HAP microparticles, the RBCs (Figure S7b) showed a similar morphology to that of native RBCs (Figure S7a). The membranes of the RBCs were smooth and the adhering of the HAP microparticles to the membrane of the RBCs was not observed.

Differing from the HAP microparticles, the HAP nanoparticles displayed some effects on the RBCs, depending on the incubation time and the surface charge. After 15 min of incubation (Figure 2a,b), a large number of the HAP nanoparticles were observed in the area surrounded by the RBCs and some HAP nanoparticles were attached on the smooth membrane of the RBCs. However, the longer incubation of 1 h with the HAP nanoparticles resulted in the formation of a sunken appearance ("caves") on the membrane surface of the RBCs, in which the HAP nanoparticles were located and membrane-bound (Figure 2c,d). Also, the highly negatively charged HAP nanoparticles were bound to the membrane of the RBCs and induced the formation of caves on the membrane surface of the RBCs (Figure 3). Whereas, the observed amount of heparin-modified HAP nanoparticles near the RBCs was much less than that of the non surface-modified HAP nanoparticles.

3.4. Adsorption capacity of HAP nanoparticles for SA. The adsorptions of SA on the HAP nanoparticles and HAP microparticles were investigated. The HAP nanoparticles exhibited a remarkably higher adsorption capacity for SA than the HAP microparticles. Figure 4**a** shows the adsorption isotherms of SA on the HAP nanoparticles and HAP microparticles, respectively. The adsorbed amount of SA on the HAP nanoparticles was linearly increased between 0.1 mg/mL and 0.6 mg/mL of SA solution and almost remained

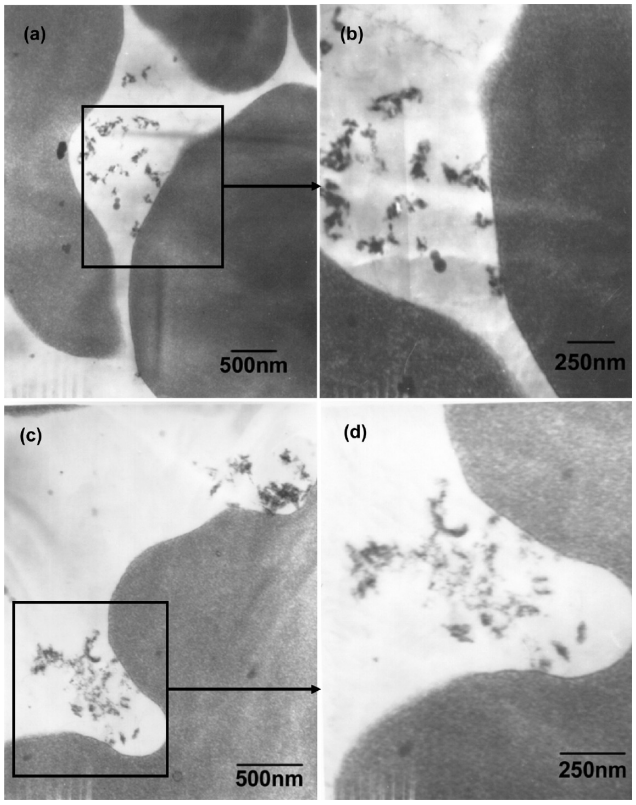

Figure 2. TEM images of RBCs incubated with HAP nanoparticles for different times. (a), (b): 15 min; (c), (d): 1 h.

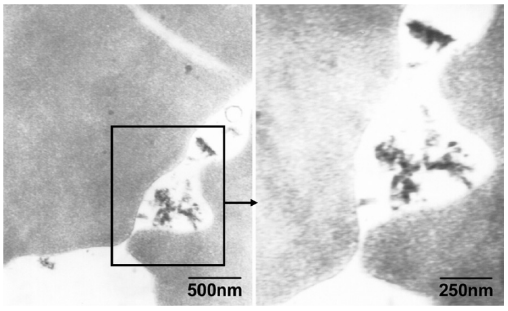

Figure 3. TEM images of RBCs incubated with heparin-modified HAP nanoparticles.

constant over 0.6 mg/mL. The maximum adsorbed amount of SA on the HAP nanoparticles was about 18 mg/g. However, the adsorbed amount of SA on the HAP microparticles was nearly not changed between 0.1 mg/mL and 0.4 mg/mL of SA solution. Then, the adsorbed amount of SA on the HAP microparticles was linearly increased in 0.4−0.8 mg/mL of SA solution and nearly not changed over 0.8 mg/mL. The maximum adsorbed amount of SA on the HAP microparticles was about 8 mg/g. The corresponding adsorption rate of SA on the HAP nanoparticles was between 35% and 55% in 0.1−1.0 mg/mL of SA solution; however, the adsorption rate of SA on the HAP microparticles was only 5−20% (Figure 4b). These results indicated that the adsorption capacity of the HAP particles was highly dependent on the particle size. In addition, the adsorption of SA on the HAP nanoparticles was lowered to some extent by the heparin surface modification of HAP nanoparticles. However, the adsorption of SA on the HAP nanoparticles was not absolutely inhibited. The maximum adsorbed amount of SA on the heparin-modified HAP nanoparticles was about 12−14 mg/g at 0.8−1.0 mg/mL of SA, corresponding to an adsorption rate of about 30% (Figure S8).

3.5. FT-IR analysis of SA adsorption on HAP nanoparticles. The FT-IR spectrum of SA (Figure 5b) showed a broad and strong band centered at 3341 cm^{-1} due to extensive N−H and O−H stretching as a result of hydrogen bonding. The O−H stretching vibrations of the −COOH group were detected at 3002, 2642, and 2519 cm^{-1}. The other vibrational bands of SA were also observed at 2933 and 2850 cm^{-1} (C−H antisymmetrical and symmetrical stretching of $-CH_3$ and $-CH_2-$), 1724 cm^{-1} (C═O stretching of −COOH), 1656 cm^{-1} (C═O stretching in $-NHCOCH_3$), 1529 cm^{-1} (N−H deformation), 1374 and 1438 cm^{-1} (symmetrical and antisymmetrical bending of $C-CH_3$), 1126 and 1263 cm^{-1} (C−O−C stretching), 1027 cm^{-1} (oxygen-containing rings).

As shown in Figure 5c, after SA adsorption, the stretching vibrations of the phosphate group and the O−H band of HAP were not changed. However, the O−H vibration of adsorbed water was moved to 3454 cm^{-1}. The magnified FT-IR spectrum showed some bands at 2927 cm^{-1}, 2856 cm^{-1}, 2526 cm^{-1}, 1734 cm^{-1}, 1716 cm^{-1}, 1660 cm^{-1}, 1641 cm^{-1}, 1628 cm^{-1}, 1556 cm^{-1}, 1541 cm^{-1}, 1450 cm^{-1} and 1425 cm^{-1}. It could be verified that the bands at 1556 cm^{-1}, 1541 cm^{-1}, 1450 cm^{-1} and 1425 cm^{-1} were attributed to the vibrations of CO_3^{2-}, and the bands at 1628 cm^{-1} and 1641 cm^{-1} were due to the vibrations of adsorbed water.[22] The bands at 2927 cm^{-1} and 2856 cm^{-1} indicated the existence of SA molecules on the surface of the HAP particles. Moreover, the bands of SA at 2519 cm^{-1} and 1656 cm^{-1} were moved to 2526 cm^{-1} and 1660 cm^{-1}, respectively, and the band at 2642 cm^{-1} disappeared. Additionally, the cleavage of the band at 1724 cm^{-1} into two peaks (1716 cm^{-1} and 1734 cm^{-1}) was also detected.

4. DISCUSSION

HAP nanoparticles exhibited size and surface effects on the aggregation of RBCs. Differing from the HAP microparticles, the HAP nanoparticles did lead to an obvious aggregation of the RBCs. However, the aggregation of the RBCs could be lowered through the use of surface modification of the HAP nanoparticles with negatively charged groups. The erythrocyte sedimentation rate was accelerated by the increasing amount of HAP nanoparticles.

The RBCs can be suspended in solution by the repulsive or disaggregating forces due to the steric and electrostatic repulsion arising from the glycocalyx of the RBCs, the membrane strain, and the mechanical shearing. Over the past few decades, the effects of different kinds of macromolecules on the aggregation of RBCs have been widely discussed. Now there are two coexisting yet mutually exclusive "models" for aggregation of RBCs −the so-called "bridging" and "depletion" models in the macromolecules solution.[23] For the bridging model, macromolecules are adsorbed onto adjacent cell surfaces resulting in the attractive bridging force. When the attractive bridging force exceeds the disaggregating forces, aggregation of the RBCs occurs.[24−26] In the depletion model, the depletion layer of the macromolecules occurs near the cell surface due to the relatively lower concentration of macromolecules in the fluid than that in the bulk solution. The merging of the depletion layers of adjacent cells can result in an attractive force. When the attractive force is sufficient to overcome the disaggregating forces, aggregation of the RBCs appears.[27−29]

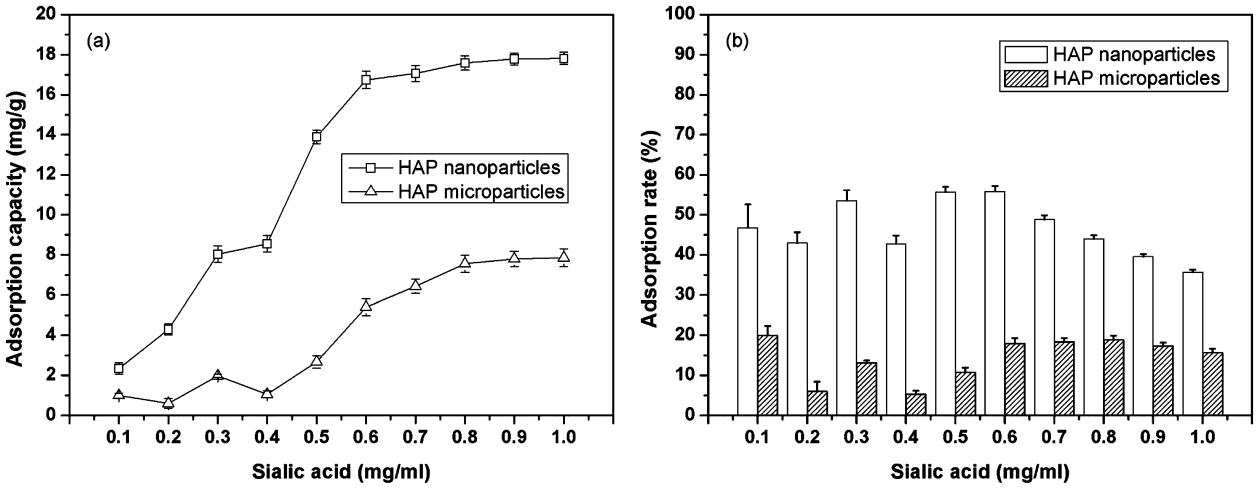

Figure 4. Adsorption isotherms (a) and adsorption rate (b) of SA on HAP nanoparticles and HAP microparticles.

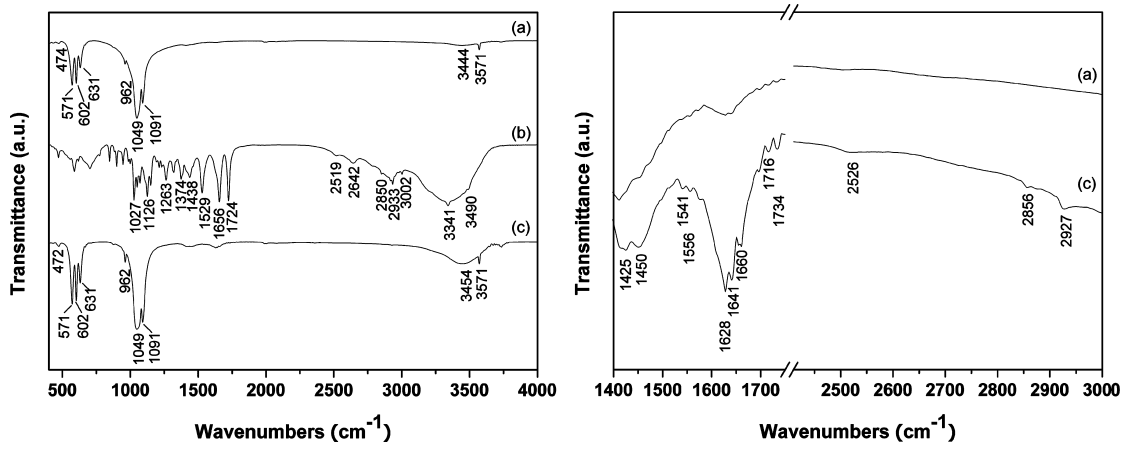

Figure 5. FT-IR spectra of HAP nanoparticles before and after adsorption of SA (left). (a) pure HAP nanoparticles; (b) SA; (c) SA adsorbed HAP nanoparticles. Right is the magnified FT-IR spectra of pure HAP nanoparticles (a) and SA adsorbed HAP nanoparticles (c).

Herein, we consult the bridging and depletion models to explain the aggregation of RBCs induced by inorganic nanoparticles. The morphologies of the aggregations of RBCs are different for the bridging model and the depletion model. The strong attractive bridging force associated with the bridging model leads to the formation of unstructured agglutinates. In contrast, with the depletion-model, the aggregating RBCs can slip freely into a face-to-face rouleaux configuration (a reduced energy configuration) after their initial contact since the attractive forces do not involve direct contact between the cell surfaces and the macromolecules. In our experiment, unstructured agglutinates of RBCs induced by the HAP nanoparticles were observed rather than the rouleaux configuration. Moreover, TEM observations also demonstrated that HAP nanocrystals could be found adhered to the membrane of the RBCs, indicating the potential bridging force between the RBCs. In addition, our results showed that the aggregations of RBCs induced by the stable heparin-modified HAP nanoparticles (about −50 mV zeta potential) were lowered due to the inhibition of the agglomeration of the HAP nanoparticles, also implying the derivation of a bridging force from the HAP nanoparticles for RBCs' aggregation. Therefore, the aggregations of RBCs induced by the HAP nanoparticles should be assigned to the bridging model.

Evidence suggests that calcium phosphate crystals could adhere to the anionic sites on the surface of renal epithelial cells.[30−32] It has also been speculated that the interaction between renal epithelial cells and HAP crystals involved negatively charged molecules protruding from the apical surface of the plasma membrane.[33,34] The studies showed that the SA residues on the cell surface were a part of the cell-crystal interface.[30,33,35] These SA residues on the cell surface could facilitate coordination with the calcium sites and water molecules on the surface of the calcium phosphate crystals in the appropriate three-dimensional organization.[36] RBCs are coated with a variety of proteins extending from the membrane surface. Many of these proteins are highly glycosylated with SA residues.[37,38] Therefore, the adsorption sites of the HAP nanoparticles on the RBCs should be focused on the interaction between the HAP nanoparticles and the SA residues protruding from the RBCs. Prior to a discussion of the adsorption sites between HAP and RBCs, the surface charge of HAP should be taken into account because the preferential adsorption of biomolecules on a hydrophilic surface is generally governed by electrostatics. Due to the emerging calcium and phosphate ions in the surface structure, HAP possesses two different binding sites on the crystal surface, the so-called C and P sites. Therefore, HAP contains multiple-site binding characteristics for biomolecules. The C site is arranged on *ac*

or *bc* crystal faces and the P site is arranged hexagonally on the *ab* crystal face. The C site is rich in calcium ions and thus binds to the acidic groups of the biomolecules, but the P site lacks calcium ions and therefore attaches to the basic groups of the biomolecules.[39] The FT-IR spectrum of HAP nanoparticles with adsorbed SA molecules provided indirect evidence to verify the interaction between the HAP nanoparticles and RBCs. Clearly, the O−H stretching vibration of −COOH at 2519 cm^{-1} moved to 2526 cm^{-1} along with the disappearance of the band at 2642 cm^{-1}, and the C═O stretching vibration of −COOH at 1724 cm^{-1} was splited into 1716 cm^{-1} and 1734 cm^{-1}, indicating the electrostatic interaction between the Ca^{2+} of HAP and the −COOH group of SA. In addition, the changes of C═O stretching vibration in $-NHCOCH_3$ revealed the potential adsorption site of SA with HAP. Also, the adsorption amount of SA on heparin-modified HAP nanoparticles was lowered; optical microscopy and TEM observations showed that the aggregation of RBCs induced by the heparin-modified HAP nanoparticles and the amount of heparin-modified HAP nanoparticles interacting with RBCs declined. This was due to the preferential binding of heparin molecules on the HAP nanoparticles via electrostatic bond formation between the negatively charged groups ($-SO_3^-$) of heparin and the positive Ca^{2+} sites on the HAP surface, which could be demonstrated by the vibrational moving of the special $-O-SO_3^-$ group of heparin adsorbed on HAP (Figure S3). Accordingly, the primary mechanism that is responsible for the adsorption of HAP to the membrane of RBCs can be assumed to be due to the electrostatic interactions between the −COOH and $-NHCOCH_3$ groups of SA and the binding sites on the HAP surface.

Due to the nano size and the large specific surface area, there should be relatively large amounts of atoms on the surface of the HAP nanoparticles and hence a large fraction of C and P sites can be expected as compared to HAP microparticles. That is to say, HAP nanoparticles can exhibit stronger interaction with RBCs than with HAP microparticles. This can be demonstrated by the higher adsorption capacity of the HAP nanoparticles (per gram) for SA than HAP microparticles, as well as their ability to achieve a stronger bridging force between the RBCs. However, for the HAP nanoparticles and HAP microparticles, the adsorbed amounts per square meter of SA were 0.129 mg/m^2 and 0.735 mg/m^2, respectively, indicating that the increased surface area of the HAP nanoparticles did not provide a similar adsorption capacity to that of the HAP microparticles. This should be attributed to the lower degree of crystallinity of the HAP nanoparticles than the HAP microparticles (Figure S2). The well−crystalline and stoichiometric HAP microparticles possess a sufficient number of C and P sites on the surface, ensuring the adsorption capacity for SA. Whereas, the HAP nanoparticles with their low degree of crystallinity, normally show a nonstoichiometric composition as well as a decreasing number of C and P sites on the surface. Victor et al. reported that HAP nanoparticles did not induce the aggregation of RBCs after 20 min of incubation.[40] The HAP nanoparticles used had a much lower degree of crystallinity with the absent characteristic absorption band of the hydroxyl group at 3572 cm^{-1}. This also implies that the degree of crystallinity of HAP as well as the crystallographic structure may affect the interaction of the HAP nanoparticles with the RBCs. Additionally, Kandori et al. studied the adsorption capacity of synthetic HAP particles, showing that the saturated amount of BSA adsorbed on the HAP particles was strongly dependent on the particle lengths rather than on the Ca/PO_4 molar ratio.[41] This was due to the specific electrostatic interaction between the negatively charged carboxylic acid groups of BSA and the positively charged C sites on the exposed ac or bc crystal faces, demonstrating the importance of the C sites of HAP for the adsorption capacity toward acidic proteins. Therefore, the degree of crystallinity and the shape of the HAP nanoparticles should be taken into account for their interactions with cells.

P. Dalal et al. studied the influence of calcium pyrophosphate dehydrate (CPPD) crystals on the phospholipid bilayer integrity using the CHARMM method of molecular dynamics simulation.[42] The model showed that an oriented, dipole-like electrostatic field distribution appeared between the interface of the CPPD crystal slab and the phospholipid bilayer, and extended deeply into the phospholipid bilayer resulting in the rupture of the lipid bilayer. This explains the pseudogout, an inflammatory disease, induced by the deposition of pathologic articular minerals near the membrane. In our study, the caves on the surface membrane of the RBCs were observed near the HAP nanoparticles. The mechanism should be similar to the rupture of the lipid bilayer induced by the CPPD crystals as shown in P. Dalal et al.'s study. However, the HAP nanoparticles did not induce the leakage of the membrane of the RBCs. This is due to the lower density of surface-charged sites on the HAP crystals than on the CPPD crystals. CPPD crystals are considered as one of the most common forms of pathologic articular minerals leading to pseudogout, where HAP crystals are not often associated with acute inflammation.[43]

HAP nanoparticles are hemocompatible, which is mainly attributed to the similar composition and structure as the inorganic component of human bones. The hemocompatibility of HAP is not dependent on the particle size although the decreasing size of the HAP particles generated some effects on the aggregation of the RBCs. Kalkura et al. reported that iron-doped nanosized HAP with a minor change in composition, also showed the same hemocompatibility to that of the nanosized HAP, indicating that the crystal structure of HAP was important for its hemocompatibility.[19] In addition, the surface property of the HAP nanoparticles was another important factor influencing their interaction with the RBCs. Our results showed that the heparin-modified HAP nanoparticles exhibited lowered aggregation of the RBCs and membrane binding. This is well consistent with the results about improving hemocompatibility of other hemolytic materials. For example, the hemocompatibility of amorphous silica materials was much improved by their surface functionalization using sulfonic and carboxy moieties;[44] the hemolytic activity of graphene oxide was nearly eliminated by coating with chitosan.[45] Consequently, the dominant factor influencing the hemocompatibility of the HAP nanoparticles should be their surface properties rather than their particle size.

5. CONCLUSIONS

HAP nanoparticles exhibited nanosize and surface charge effects on the aggregation of RBCs in RBC suspensions. Differing from HAP microparticles, the HAP nanoparticles resulted in the aggregation of the RBCs with the unstructured agglutinates (bridging model). Electrostatic interactions between the positively charged binding sites on the HAP surface and the negatively charged groups on the surface of the RBCs, caused the HAP nanoparticles to adhere to the

membrane of the RBCs and bridging force being generated between the RBCs. The aggregation of the RBCs induced by the HAP nanoparticles was lowered by surface modification of the HAP nanoparticles with negatively charged groups. Although adhering of the HAP nanoparticles to the membrane of each of the RBCs led to the formation of caves on the membrane, hemolysis was not observed. The dominant factor influencing the hemocompatibility of the HAP nanoparticles was the surface properties of the HAP nanoparticles rather than their particle size.

■ ASSOCIATED CONTENT

Supporting Information

TEM images, XRD patterns and FT-IR spectra of HAP nanoparticles, heparin-modified HAP nanoparticles and HAP microparticles; FT-IR spectrum of heparin; Size distribution and zeta potential of heparin-modified HAP nanoparticles; Effect of concentration of heparin-modified HAP nanoparticles on the erythrocyte sedimentation rate; TEM images of RBCs after 1 h incubation without HAP particles and with HAP microparticles; Adsorption isotherm and rate of SA on heparin-modified HAP nanoparticles. This material is available free of charge via the Internet at http://pubs.acs.org.

■ AUTHOR INFORMATION

Corresponding Author

*Address: Biomedical Materials and Engineering Center of Wuhan University of Technology, 122 Luoshi Road, Hongshan, Wuhan 430070, Hubei, P. R. China. E-mail: hanyingchaowhut@yahoo.cn. Tel.: +86-27-87651852. Fax: +86-27-87880734.

Notes

The authors declare no competing financial interest.

■ ACKNOWLEDGMENTS

This work was supported by grants from the National Natural Science Foundation of China (51002109, 81190133 & 51172171), the Natural Science Foundation of Hubei Province of China (2009CDA041), the Science and Technology Project of Wuhan (201060938362-02) and the Fundamental Research Funds for the Central Universities. Yingchao Han is grateful to the PCSIRT.

■ REFERENCES

(1) Brigger, I.; Dubernet, C.; Couvreur, P. *Adv. Drug. Deliv. Rev.* **2002**, *54*, 631−651.
(2) McNeil, S. E. *J. Leukocyte Biol.* **2005**, *78*, 585−594.
(3) LeGeros, R. Z.; LeGeros, J. P. *Key Eng. Mater.* **2003**, *240*−*242*, 3−10.
(4) Edward, S. A.; Nathaniel, J. G.; Atsushi, N.; Jackie, Y. Y. *Nano Lett.* **2001**, *1*, 149−153.
(5) Sung, Y. M.; Lee, J. C.; Yang, J. W. *J. Cryst. Growth* **2004**, *262*, 467−472.
(6) Meyers, M. A.; Mishra, A.; Benson, D. J. *Prog. Mater. Sci.* **2006**, *51*, 427−556.
(7) Ramesh, S.; Tan, C. Y.; Sopyan, I.; Hamdi, M.; Teng, W. D. *Sci. Technol. Adv. Mater.* **2007**, *8*, 124−130.
(8) Webster, T. J.; Ergun, C.; Doremus, R. H.; Siegel, R. W.; Bizios, R. *Biomaterials* **2001**, *22*, 1327−1333.
(9) Li, H.; Khor, K. A.; Chow, V.; Cheang, P. *J. Biomed. Mater. Res. Part A* **2007**, *82*, 296−303.
(10) Kohsuke, M.; Takayoshi, H.; Tomoo, M.; Kohki, E.; Kiyotomi, K. *J. Am. Chem. Soc.* **2004**, *126*, 10657−10666.
(11) Roy, I.; Mitra, S.; Maitra, A.; Mozumdar, S. *Int. J. Pharm.* **2003**, *250*, 25−33.
(12) Ferraz, M. P.; Mateus, A. Y.; Sousa, J. C.; Monteiro, F. J. *J. Biomed. Mater. Res. Part A* **2007**, *81*, 994−1004.
(13) Tada, S.; Chowdhury, E. H.; Cho, C. S.; Akaike, T. *Biomaterials* **2010**, *31*, 1453−1459.
(14) Giger, E. V.; Puigmartí-Luis, J.; Schlatter, R.; Castagner, B.; Dittrich, P. S.; Leroux, J. C. *J. Controlled Release* **2011**, *150*, 87−93.
(15) Lebugle, A.; Pellé, F.; Charvillat, C.; Rousselot, I.; Chane-Ching, J. Y. *Chem. Commun.* **2006**, *14*, 606−608.
(16) Mondéjar, S. P.; Kovtun, A.; Epple, M. *J. Mater. Chem.* **2007**, *17*, 4153−4159.
(17) Han, Y. C.; Wang, X. Y.; Li, S. P. *Curr. Nanosci.* **2010**, *6*, 178−183.
(18) Han, Y. C.; Li, S. P.; Wang, X. Y.; Chen, X. M. *Mater. Res. Bull.* **2004**, *39*, 25−32.
(19) Chandra, V. S.; Baskar, G.; Suganthi, R. V.; Elayaraja, K.; Joshy, M. I.; Beaula, W. S.; Mythili, R.; Venkatraman, G.; Kalkura, S. N. *ACS Appl. Mater. Interfaces* **2012**, *4*, 1200−1210.
(20) Seaman1, G. V. F.; Uhlenbruck, G. *Arch. Biochem. Biophys.* **1963**, *100*, 493−502.
(21) Carradó, A. *ACS Appl. Mater. Interfaces* **2010**, *2*, 561−565.
(22) Bertinetti, L.; Tampieri, A.; Landi, E.; Ducati, C.; Midgley, P. A.; Coluccia, S.; Martra, G. *J. Phys. Chem. C* **2007**, *111*, 4027−4035.
(23) Armstrong, J. K.; Wenby, R. B.; Meiselman, H. J.; Fisher, T. C. *Biophys. J.* **2004**, *87*, 4259−4270.
(24) Brooks, D. E. *J. Colloid Interface Sci.* **1973**, *43*, 700−713.
(25) Brooks, D. E. In *Mechanism of red cell aggregation. In Blood Cells, Rheology and Aging*; Platt, D., Ed; Springer Verlag: Berlin, 1988; p 158−162.
(26) Chien, S.; Lang, L. A. *Clin. Hemorheol.* **1987**, *7*, 71−91.
(27) van Oss, C. J.; Arnold, K.; Coakley, W. T. *Cell Biophys.* **1990**, *17*, 1−10.
(28) Baümler, H.; Neu, B.; Donath, E.; Kiesewetter, H. *Biorheology* **1999**, *36*, 439−442.
(29) Baümler, H.; Neu, B.; Mitlohner, R.; Georgieva, R.; Meiselman, H. J.; Kiesewetter, H. *Biorheology* **2001**, *38*, 39−51.
(30) Lieske, J. C.; Norris, R.; Toback, F. G. *Am. J. Physiol.* **1997**, *273*, F224−F233.
(31) Sayer, J. A.; Carr, G.; Simmons, N. L. *Clin. Sci.* **2004**, *106*, 549−561.
(32) Vervaet, B. A.; D'Haese, P. C.; Broe, M. E. D.; Verhulst, A. *Nephrol. Dial. Transplant.* **2009**, *24*, 3659−3668.
(33) Lieske, J. C.; Leonard, R.; Swift, H.; Toback, F. G. *Am. J. Physiol.* **1996**, *270*, F192−F199.
(34) Dalal, P.; Zanotti, K.; Wierzbicki, A.; Madura, J. D.; Cheung, H. S. *Biophys. J.* **2005**, *89*, 2251−2257.
(35) Lieske, J. C.; Toback, F. G.; Deganello, S. *Kidney Int.* **2001**, *60*, 1784−1791.
(36) Verkoelen, C. F.; van der Boom, B. G.; Kok, D. J.; Romijn, J. C. *Kidney Int.* **2000**, *57*, 1072−1082.
(37) Moghimi, S. M.; Hedeman, H.; Muir, I. S.; Illum, L.; Davis, S. S. *Biochim. Biophys. Acta* **1993**, *1157*, 233−240.
(38) Chambers, E.; Mitragotri, S. *J. Controlled Release* **2004**, *100*, 111−119.
(39) Kandori, K.; Fudo, A.; Ishikawa, T. *Phys. Chem. Chem. Phys.* **2000**, *2*, 2015−2020.
(40) Victor, S. P.; Sharma, C. P. *Colloid Surf. B-Biointerfaces* **2011**, *85*, 221−228.
(41) Kandori, K.; Fudo, A.; Ishikawa, T. *Phys. Chem. Chem. Phys.* **2000**, *2*, 2015−2020.
(42) Dalal, P.; Zanotti, K.; Wierzbicki, A.; Madura, J. D.; Cheung, H. S. *Biophys. J.* **2005**, *89*, 2251−2257.
(43) Wierzbicki, A.; Dalal, P.; Madura, J. D.; Cheung, H. S. *J. Phys. Chem.B* **2003**, *107*, 12346−12351.
(44) Slowing, I. I.; Wu, C.-W.; Vivero-Escoto, J. L.; Victor, S.-Y. L. *Small* **2009**, *5*, 57−62.
(45) Liao, K.-H.; Lin, Y.-S.; Macosko, C. W.; Haynes, C. L. *ACS Appl. Mater. Interfaces* **2011**, *3*, 2607−2615.